

Image Field Categorization and Edge/Corner Detection from Gradient Covariance

Shigeru Ando, *Member, IEEE*

Abstract—Edges, corners, and vertices in an image correspond to 1D (one-dimensional) and 2D discontinuities in the intensity surface of the underlying scene. Ridges and peaks correspond to 1D and 2D extrema in it. All of them can be characterized by the distribution of gradients, particularly by dimensionality of it. The approach to image field categorization here is to construct a covariance matrix of the gradient vector in each small window and apply the canonical correlation analysis to it. Schwarz's inequality on the matrix determinant and the related differential equation is the key to this analysis. We obtain two operators P_{EG} and Q_{EG} to categorize the image field into a unidirectionally varying region (UNIVAR), an omnidirectionally varying region (OMNIVAR), and a nonvarying region. We investigate the conditions under which their absolute maximum response, i.e., $P_{EG} = 1$ and $Q_{EG} = 1$, occurs in the small window and show that they are, respectively, the desired 1D and 2D discontinuities/extrema and OMNIVAR, in many cases, a 1D pattern in polar coordinates. This leads to an algorithm to obtain further classification and accurate localization of them into edges, ridges, peaks, corners, and vertices through detailed analysis in the informative (varying) axis of them. We examined and compared the performance of the operators and the localization algorithm on various types of images and various noise levels. The results indicate that the proposed method is superior with respect to stability, localization, and resolution.

Index Terms—Image feature extraction, edge, corner, vertex, gradient covariance.

1 INTRODUCTION

FEATURE extraction is one of the most important areas of image analysis and computer vision. A great deal of effort has been spent on this problem, in particular, on the problem of edge and corner detection. Various approaches to detecting these feature points have been reported in the extensive literatures over a few decades; broadly, these approaches can be divided into several groups.

The first group is based on the edge strength, which is computed locally by specific linear or nonlinear operators. It includes Rosenfeld and Thurston's method [1] for grayness and texture features, Robinson's orientation masks [2], Frei and Chen's edge consistency measure [3], Shanmugam et al.'s optimum Fourier domain filter [4], the Nevatia and Babu [5] operators followed by thinning and thresholding, Marr and Hildreth's Laplacian of Gaussian filter followed by the zero-cross detection [6], the Canny operator [7] which maximizes the signal-to-noise ratio and minimizes the localization error and the spurious responses, Ramponi's second-order Volterra filter [8], and Kisworo et al.'s instantaneous energy detector [9]. These methods, however, are seen to be much too dependent on the performance of operators which must convert diverging variation of image pattern into a scalar value. They often yield noisy results, hence powerful, intermediate-level processes are required.

The second group of edge detection methods is often called orientation analysis. It lays more stress on the orientation of a gradient rather than its strength. It includes Machuca and Gilbert's step edge and roof edge detector [10], Zuniga and Haralick's

directional derivative operators [11], Gregson's angular dispersion operator [12], and Martens method of using the Hermite transform [13]. These methods rely on the coherency of gradient direction near edges, hence they are invariant with grayness dimension (contrast). The problem, however, is the lack of a method to extract reliable direction from potentially noisy images.

The third group is based on fitting or matching of particular models to the image field. It includes Brooks' method of fitting a plane or a quadric [14], Haralick's method of fitting a cubic facet and detecting a zero cross of second order derivative [15], Tabatabai and Mitchell's method of fitting an ideal edge by preserving first, second, and third order moments [16], Nalwa and Binford's method of fitting a one-dimensional surface [17], Ghosal and Mehrotra's method of fitting a generalized step edge or a pulse edge using Zernike moments [18], and Chen and Yang's method of fitting a B-spline with regularization [19]. This type of approach, however, can sometimes fail when the assumption underlying those models is unsuitable.

Corners and vertices represent another class of information in image analysis. These features can be used to identify objects in the scene, for example, for stereoscopic matching, geometrical calibration, because of their accurate and less ambiguous localization. Several approaches to the detection of these feature points have been reported: five methods by Kitchen and Rosenfeld [20], including the Beaudet *DET* operator, the use of Plessey corner detector by Noble [21], [24], the use of the matched filter corner detector by Rangarajan et al. [22], the use of some cornerity measures by Singh and Shneider [23], the use of a dissimilarity measure of edge shape from surrounds by Cooper et al. [25], and the use of Zernike moment by Ghosal and Mehrotra [26]. Another approach is the use of nonlinear differential geometric operators for the scale-space analysis. It includes critical points of the gradient field used by Machuca and Phillips [27], the scale-space invariants, particularly ridges and valleys used by Florack et al. [28], and the maximum curvature and isophotes used by Maintz et al. [29]. A common problem encountered in these methods is the choice of Gaussian smoothing necessary to compute higher order derivatives without magnifying noise. In this sense, a novel approach is the SUSAN method by Smith and Brady [31], which does not rely on gradients, hence it is robust against noise. For comparisons of the performance of these operators or algorithms, see Deutsch and Fram [32], Peli and Malah [33], Delp and Chu [34], Lyvers and Mitchell [35], Fleck [36], Kakarala and Hero [37], Koplowitz and Greco [38], Ganesan and Bhattacharyya [39], Pedersini et al. [40], and Heath et al. [41].

In this paper, we propose a two-stage paradigm of image feature extraction. Both stages are nonparametric and perform treelike categorization. The first stage is the categorization of an image field into a unidirectionally varying region (UNIVAR), an omnidirectionally varying region (OMNIVAR), and other regions. Since OMNIVAR is also unidirectionally varying in polar coordinates, the second stage is devoted to detailed analysis along the informative axis of UNIVAR and OMNIVAR to localize edge/ridge and peak/corner/vertex, respectively. The origin of our operators is the use of the Gaussian curvature of correlation function for texture analysis [42], [43]. It was first proposed by us as texton finders and has been developed as the integrated feature extractors of the "SmartHead" sensor [44], [45]. In spite of their statistical background, the operators were found to become more efficient when the window became very small. This motivated the UNIVAR/OMNIVAR categorization approach of local image features. A well-known operator in the same class in computer vision is the Plessey corner detector [21]; it uses a spatial average of an outer product of the gradient vector, which is equivalent to the gradient covariance of our method. The difference between it and

• The author is with the Department of Mathematical Engineering and Information Physics, Graduate School of Engineering, The University of Tokyo, 7-3-1 Hongo, Bunkyo-ku, Tokyo 113-8656 Japan.
E-mail: ando@alab.t.u-tokyo.ac.jp.

Manuscript received 7 Nov. 1998; accepted 16 Nov. 1999.

Recommended for acceptance by M. Shah.

For information on obtaining reprints of this article, please send e-mail to: tpami@computer.org, and reference IEEECS Log Number 107520.

our operators, both in theory and in application framework, will be clarified in this paper.

2 IMAGE FIELD CATEGORIZATION FROM GRADIENT COVARIANCE

In the following argument, we assume that the integration area Γ is sufficiently small (e.g., from 3×3 pixels to 5×5 pixels). Therefore, we cannot deal with any of the correlation integrals below as converged statistical quantities. We also assume that the image is continuously differentiable everywhere.¹

2.1 UNIVAR Detector and OMNIVAR Detector

Let us consider cross correlations between f_x and f_y as

$$\begin{aligned} \left\langle \begin{bmatrix} f_x \\ f_y \end{bmatrix} \begin{bmatrix} f_x f_y \end{bmatrix} \right\rangle &= \begin{bmatrix} \langle f_x^2 \rangle & \langle f_x f_y \rangle \\ \langle f_y f_x \rangle & \langle f_y^2 \rangle \end{bmatrix} \\ &= \begin{bmatrix} S_{xx} & S_{xy} \\ S_{xy} & S_{yy} \end{bmatrix}, \end{aligned} \quad (1)$$

where

$$\langle \cdot \rangle \equiv \iint_{\Gamma} \cdot \, dxdy \quad (2)$$

means an integral in the small region Γ . Let λ be an eigenvalue of this matrix. Since it is a solution of

$$\begin{aligned} \begin{vmatrix} S_{xx} - \lambda & S_{xy} \\ S_{xy} & S_{yy} - \lambda \end{vmatrix} &= (S_{xx} - \lambda)(S_{yy} - \lambda) - S_{xy}^2 \\ &= \lambda^2 - (S_{xx} + S_{yy})\lambda + S_{xx}S_{yy} - S_{xy}^2 \\ &= 0, \end{aligned} \quad (3)$$

two eigenvalues λ_1, λ_2 of the matrix satisfy

$$\lambda_1 + \lambda_2 = S_{xx} + S_{yy} > 0, \quad \lambda_1 \lambda_2 = S_{xx}S_{yy} - S_{xy}^2 > 0, \quad (4)$$

and its discriminant is

$$\begin{aligned} (S_{xx} + S_{yy})^2 - 4(S_{xx}S_{yy} - S_{xy}^2) &= (S_{xx} - S_{yy})^2 + 4S_{xy}^2 \\ &\geq 0. \end{aligned} \quad (5)$$

This means that both λ_1, λ_2 are real and nonnegative.² Actually, λ_1, λ_2 are variances of two principal components of the (f_x, f_y) distribution. By using them, we can define the homogeneity measure

$$Q_{EG} = \left\{ \frac{\sqrt{\lambda_1 \lambda_2}}{(\lambda_1 + \lambda_2)/2} \right\}^2 = \frac{4(S_{xx}S_{yy} - S_{xy}^2)}{(S_{xx} + S_{yy})^2} \quad (6)$$

of the distribution, by taking the ratio of the multiplicative average of λ_1, λ_2 to their additive average. Since

$$0 \leq \sqrt{\lambda_1 \lambda_2} \leq \frac{\lambda_1 + \lambda_2}{2} \quad (\lambda_1, \lambda_2 > 0), \quad (7)$$

Q_{EG} is dimensionless and normalized such that

$$0 \leq Q_{EG} \leq 1. \quad (8)$$

1. The optical image is, in itself, band-limited, hence, theoretically, f is differentiable everywhere. In practice, we use Gaussian smoothing to reduce discretization noise.

2. All eigenvalues of the covariance matrix are real and nonnegative because it is Hermitian and positive semidefinite.

Let us define a complementary measure of Q_{EG} as

$$P_{EG} \equiv 1 - Q_{EG} = \frac{(S_{xx} - S_{yy})^2 + 4S_{xy}^2}{(S_{xx} + S_{yy})^2}, \quad (9)$$

which is also dimensionless and normalized such that

$$0 \leq P_{EG} \leq 1. \quad (10)$$

We name P_{EG} and Q_{EG} a UNIVAR Detector and an OMNIVAR Detector, respectively, because they have the following properties.

Theorem 1.

1. P_{EG} reaches 1 where the grayness varies one-dimensionally.
2. Q_{EG} reaches 1, where the grayness variation is omnidirectional in such a sense that

$$S_{xx} = S_{yy}, \quad S_{xy} = 0. \quad (11)$$

The proof is shown in the Appendix. To clarify these properties, and remove the condition that, $P_{EG}=0/0, Q_{EG}=0/0$ if the image is completely flat in Γ , it is useful to modify the definitions of P_{EG} and Q_{EG} as follows: Since $S_{xx}+S_{yy}$ is the total variance of the gradient in Γ , we add a small constant σ_{EG}^4 to it in the denominator in such a way that

$$P_{EG} = \frac{(S_{xx} - S_{yy})^2 + 4S_{xy}^2}{(S_{xx} + S_{yy})^2 + \sigma_{EG}^4} \quad (12)$$

$$Q_{EG} = \frac{4(S_{xx}S_{yy} - S_{xy}^2)}{(S_{xx} + S_{yy})^2 + \sigma_{EG}^4}, \quad (13)$$

to remove the 0/0 condition. Through this modification, both P_{EG} and Q_{EG} are forced to be zero if $S_{xx}+S_{yy}$ is significantly smaller than σ_{EG}^2 . Therefore, σ_{EG}^2 , in a sense, is the threshold value of grayness variation which should be classified by P_{EG} or Q_{EG} .

From Theorem 1, we can readily observe the following properties of P_{EG} and Q_{EG} :

Observation 1.

1. P_{EG} reaches 1 in "slants" of grayness.
2. P_{EG} reaches 1 near edges or ridges.
3. Q_{EG} reaches 1 at a center of circular symmetry.
4. Q_{EG} reaches 1 at a center of rotational periodicity with a period $\pi/2$.
5. Q_{EG} reaches 1 at a center of rotational "skew periodicity" with a period $\pi/2$.

The proofs are shown in the Appendix. By "slants", we mean a grayness pattern which is approximated locally (in an area as wide as Γ) by

$$f(x, y) = px + qy + r, \quad \sqrt{p^2 + q^2} \gg 0, \quad (14)$$

and, by edge and ridge, we mean grayness patterns which have following local properties.

1. Across a line, they show rapid change of grayness the cross section of which is like a step or a ridge,
2. The change in the shape of the cross sections along the line is small.

By the rotational periodicity with a period $\pi/2$, we mean a grayness pattern which satisfies

$$f\left(r, \theta + \frac{n\pi}{2}\right) = f(r, \theta) \quad (15)$$

$$f_r\left(r, \theta + \frac{n\pi}{2}\right) = f_r(r, \theta) \quad (16)$$

$$f_\theta\left(r, \theta + \frac{n\pi}{2}\right) = f_\theta(r, \theta), \quad (17)$$

and by “skew-periodicity” we mean

$$f\left(r, \theta + \frac{n\pi}{2}\right) + f_0 = (-1)^n f(r, \theta) + f_0 \quad (18)$$

$$f_r\left(r, \theta + \frac{n\pi}{2}\right) = (-1)^n f_r(r, \theta) \quad (19)$$

$$f_\theta\left(r, \theta + \frac{n\pi}{2}\right) = (-1)^n f_\theta(r, \theta), \quad (20)$$

where f_0 is a properly chosen constant.

From 3 of this observation, we expect Q_{EG} to detect the centers of a dot or blob in an image. From 4 and 5, we also expect that it will respond at orthogonal intersection of lines or edges. This means that OMNIVAR frequently appears in unidirectionally varying regions in polar coordinates such as peaks, corners, and vertices.

2.2 Orientation and Strength Attributes

From (3), we can readily solve the eigenvalues

$$\lambda = \frac{S_{xx} + S_{yy} \pm \sqrt{(S_{xx} - S_{yy})^2 + 4S_{xy}^2}}{2}, \quad (21)$$

and corresponding eigenvectors (unnormalized)

$$\begin{bmatrix} -S_{xy} \\ S_{xx} - \lambda \end{bmatrix} = \begin{bmatrix} -S_{xy} \\ S_{xx} - S_{yy} \mp \sqrt{(S_{xx} - S_{yy})^2 + 4S_{xy}^2} \end{bmatrix}. \quad (22)$$

The normal direction of an edge or ridge is equal to a direction of eigenvectors with the largest eigenvalue. Therefore, it is expressed as

$$\theta_{EG} = \tan^{-1} \frac{S_{xx} - S_{yy} - \sqrt{(S_{xx} - S_{yy})^2 + 4S_{xy}^2}}{-2S_{xy}}. \quad (23)$$

Let us define strength measures

$$U_{EG} = (S_{xx} - S_{yy})^2 + 4S_{xy}^2 \quad (24)$$

$$V_{EG} = 4(S_{xx}S_{yy} - S_{xy}^2) \quad (25)$$

$$W_{EG} = (S_{xx} + S_{yy})^2. \quad (26)$$

Then,

$$U_{EG} + V_{EG} = W_{EG}, \quad (27)$$

and, from definitions in (9) and (6),

$$P_{EG} = \frac{(S_{xx} - S_{yy})^2 + 4S_{xy}^2}{(S_{xx} + S_{yy})^2} = \frac{U_{EG}}{W_{EG}} \quad (28)$$

$$Q_{EG} = \frac{4(S_{xx}S_{yy} - S_{xy}^2)}{(S_{xx} + S_{yy})^2} = \frac{V_{EG}}{W_{EG}}. \quad (29)$$

This implies that W_{EG} can be regarded as a total “energy” of grayness variation, which is decomposed additively into U_{EG} and V_{EG} according to the ratio of P_{EG} to Q_{EG} . From this view, the Plessey corner detector [21] is expressed as

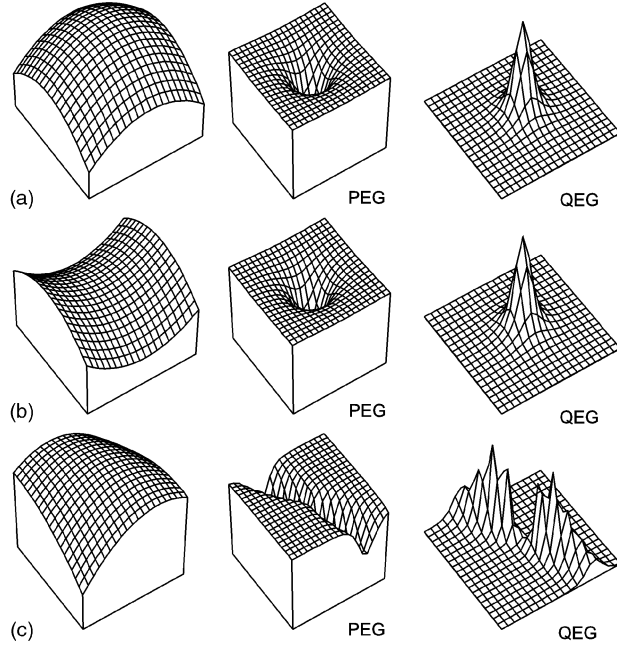


Fig. 1. Simulation results of P_{EG} and Q_{EG} for blob and saddle patterns. For each row, the leftmost diagram is an original grayness pattern and those to its right show the response to it. The Γ size is 3×3 pixels.

$$C_p \equiv \frac{S_{xx} + S_{yy}}{S_{xx}S_{yy} - S_{xy}^2} = \frac{\sqrt{W_{EG}}}{V_{EG}/4} = \frac{4}{\sqrt{W_{EG}}} \cdot \frac{1}{Q_{EG}}, \quad (30)$$

which is equivalent to an inverse of Q_{EG} weighted by a root-mean-square of the total grayness variation.

2.3 Remarks

2.3.1 Benefit of Normalization

The proposed operators P_{EG} and Q_{EG} are normalized within $[0, 1]$. For features with sufficient SNR, i.e., $S_{xx} + S_{yy} \gg \sigma_{EG}^2$, they are exactly dimensionless. This means that they acquire improved independence from physical conditions in which the image was taken. Therefore, they provide suitable representation for the comparison of different images which were taken under different conditions of illumination, distance, size, and orientation. Possible applications are the so-called interest operators for image data retrieval. In this sense, the results of experiments by Schmid and Mohr [30] are encouraging, which showed that the Plessey corner detector, which has properties similar to our Q_{EG} operator, was most effective. Another benefit of the normalization is the advanced degree of abstraction toward logical quantities. They will provide more suitable forms for fusing the image features with other information in intermediate-level vision.

2.3.2 Two Kinds of “Resolution”

The operators P_{EG} and Q_{EG} have two major factors that determine the spatial resolution property. The one is controlled by the resolution of gradient operation, i.e., sensitivity to fine (high-frequency) structures versus coarse (low-frequency) structures. If the two structures are superposed, the coarser ones are ignored or may disturb the finer ones. We can use a multiresolution framework to extract the two structures separately. This is not the case, however, when they are spatially isolated and, thus, extracted equally due to the scale invariance of the operators. The second factor is controlled by the size of Γ . It specifies a spatial extent of patterns. When Γ is very small, microscopic features such as edgels, ridges, and peaks are extracted. When it becomes larger, regular structures such as stripes, corners, and vertices are

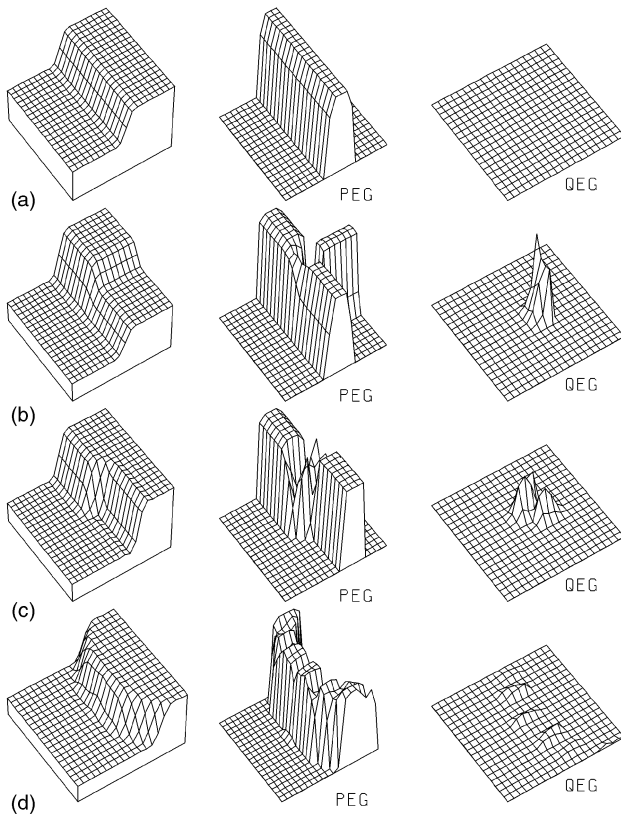


Fig. 2. Simulation results of P_{EG} and Q_{EG} for various edge patterns. For each row, the leftmost diagram is an original grayness pattern and those to its right show the response to it. The Γ size is 3×3 pixels.

extracted. When it becomes very large, statistic features such as coarseness and texture orientation are extracted [42], [43]. This shows that the proposed operators can be applied “seamlessly” to both deterministic and statistic features according to a choice of the Γ size.

2.4 Numerical Simulation

In this subsection, we illustrate to various synthetic patterns the responses of P_{EG} and Q_{EG} . For all patterns, the grayness range is $[0, 255]$ and the Γ size is 3×3 pixels.

2.4.1 Response to Blobs and Saddles

We first consider blobs and saddles shown on the extreme left of Fig. 1a, Fig. 1b, and Fig. 1c. The values of P_{EG} and Q_{EG} from each pattern are indicated by the height. The center of blob and saddle is localized very sharply by Q_{EG} and the slope around it indicated by $P_{EG} \simeq 1$. At an anisotropic peak, the response becomes weaker on the center but the response on its shoulders remains considerably.

2.4.2 Response to Step Edges

We then consider step edges shown in Fig. 2a, Fig. 2b, Fig. 2c, Fig. 2d. For a straight edge (Fig. 2a), P_{EG} has a response equal to unity and Q_{EG} has no response. The width of the responding zone is about 5, which is equal to the sum of edge width 2 and Γ size 3. For a junction of edges (T-type vertex), P_{EG} shows a unity response along both edges despite their step sizes being different. At a junction, Q_{EG} shows a sharp response within a height near 1. For an edge with a bump (Fig. 2c), the response of P_{EG} drops at the bump, while Q_{EG} rises there. For a curved edge (Fig. 2d), P_{EG} responds strongly along the curve, but Q_{EG} also has small response due to curvature and discretization error.

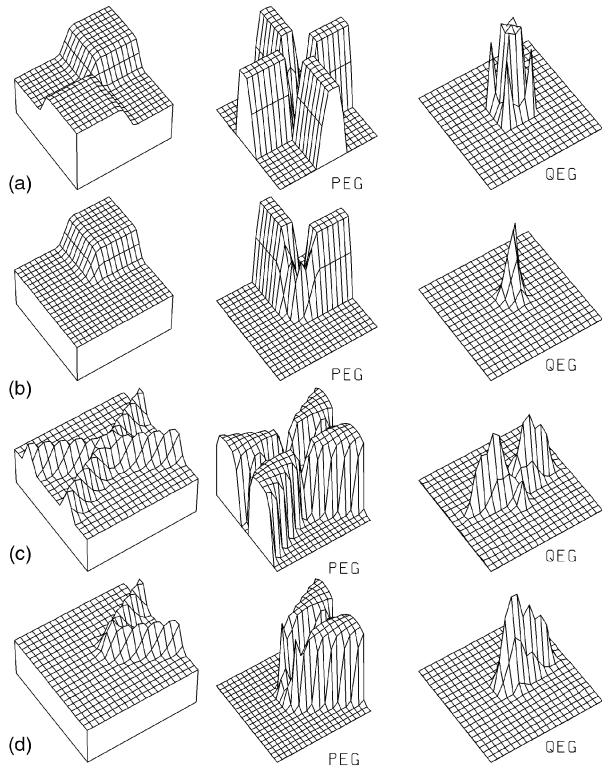


Fig. 3. Simulation results of P_{EG} and Q_{EG} for various corner patterns. For each row, the leftmost diagram is the original grayness pattern and those to its right show the response to it. The Γ size is 3×3 pixels and $\sigma_{EG}^2 = 3^2 \cdot 0.5^2$.

2.4.3 Response to Corners and Vertices

We now consider various corner/vertex/junction patterns shown in Fig. 3a, Fig. 3b, Fig. 3c, and Fig. 3d. For an X-type junction pattern (Fig. 3a), Q_{EG} has a response equal to unity at the center of the junction. This is because an image surface at the center is like a saddle whose curvatures are equal but have different signs, as well as because the pattern around it is rotationally skew periodic with a period $\pi/2$. The responding area is about 2×2 , which is roughly equal to the edge width 2. Note that four sharp peaks appear around it. They can be seen as “corner response” (see Fig. 3b) for each corner meeting at the junction. For a corner pattern (Fig. 3b), the response of Q_{EG} is very sharp, although it does not reach unity. The peak is not at the corner tip (intersection of edge lines) but near the end of the flat segment. Compare with the four “corner responses” in Fig. 3a. For a junction of ridges (Fig. 3c), Q_{EG} shows a strong response near the intersection. Since the intersection is not rectangular, the response at the center of symmetry does not reach unity. Rather, the dominant responses appear at two corners with an acute angle. Note also the thickness of the responding zone of P_{EG} . Along a ridge, UNIVAR extracted by P_{EG} is a union of responses to one ridge and two edges at both sides. At a folded ridge (Fig. 3d), Q_{EG} shows a strong response near unity at the corner. However, the peak is not at the corner tip (intersection of ridge lines). The offset is directed to a side with an acute angle.

2.4.4 Robustness against Noise

We have added Gaussian noise to a synthetic image of straight edges with different step sizes and different noise levels, as shown in Fig. 4a, Fig. 4b, Fig. 4c, and Fig. 4d. For Fig. 4a (ideal edges without noise), the response of P_{EG} is the same and strongly saturated to unity at all edges. For Fig. 4b (edges contaminated by noise with variance 0.5^2), it becomes rounded (weakly saturated to unity) at the weakest edge, while the response of Q_{EG} is almost

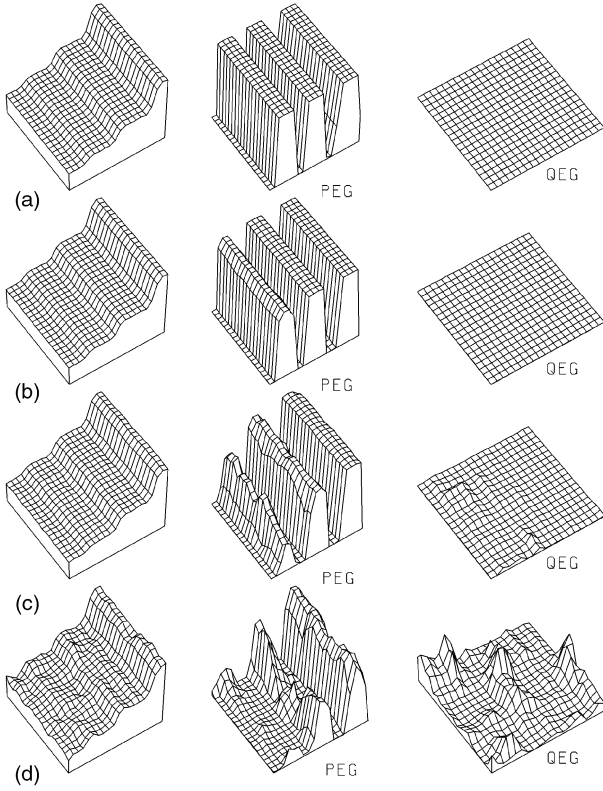


Fig. 4. Simulation results of P_{EG} and Q_{EG} for edge patterns with different step sizes and noise levels. For each row, the leftmost diagram is the original grayness pattern and the ones to its right show the response to it. The Γ size is 3×3 pixels. (a) Ideal edges without noise. (b) Edges contaminated by noise with variance 0.5^2 (~ 8 -bit quantization noise). (c) Edges contaminated by noise with variance 2.0^2 (~ 6 -bit quantization noise). (d) Edges contaminated by noise with variance 8.0^2 (~ 4 -bit quantization noise). The normalized response of P_{EG} is corrupted by noise as the decrease of S/N ratio.

zero. However, for Fig. 4c (edges contaminated by noise with variance 2.0^2) and Fig. 4d (edges contaminated by noise with variance 8.0^2), the response of P_{EG} becomes degraded or disappears and, instead, the response of Q_{EG} rises according to an increase of the noise level against the step size.

3 FURTHER CLASSIFICATION AND LOCALIZATION

In this section, we describe a method of obtaining detail description of UNIVAR and OMNIVAR, making use of the directional property of them.

3.1 Edge/Ridge Localization by Gradient Projection

The objectives of this procedure are 1) classification of UNIVAR into edge and ridge, 2) their accurate localization, and 3) to give further attributes, such as polarity of the edge and curvature, which are lost in the gradient covariance features. We propose a method based on the projection of directional gradients because:

1. It is an informative axis of UNIVAR,
2. The projection improves SNR of the informative axis without smearing,
3. Projecting gradients instead of graynesses has significant compatibility with our method in which arrays of gradients are always ready to be accessed [44], and
4. Conventional cubic fitting to the grayness [15] is achieved simply by quadratic fitting to the gradient.

For edge/ridge localization, the implementation basically consists of the following steps:

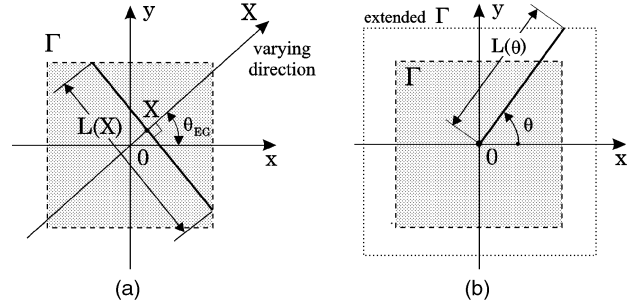


Fig. 5. Definition of projection geometry for (a) gradient projection for edge/ridge detection and (b) angular gradient projection for corner/vertex detection.

3.1.1 Gradient Projection

We can obtain the direction of the most varying axis from (23). Since the axis of projection X and the gradient component to direction X are expressed as

$$X = x \cos \theta_{EG} - y \sin \theta_{EG} \quad (31)$$

$$f_X = f_x \cos \theta_{EG} - f_y \sin \theta_{EG}, \quad (32)$$

we can compute the gradient projection as

$$\bar{f}_X(X) = \frac{1}{L(X)} \int_{L(X)} (f_x \cos \theta_{EG} - f_y \sin \theta_{EG}) dY. \quad (33)$$

The definition of $L(x)$ is expressed in Fig. 5a. Obtaining them discretely on $X = -1$, $X = 0$, and $X = 1$ is sufficient. The bilinear interpolation is used for f_x and f_y on off-grid points.

3.1.2 Localization of Edge from Extremum

The gradient extremum is detected where either

$$0 \ll \bar{f}_X(-1) \ll \bar{f}_X(0), \quad \bar{f}_X(0) \gg \bar{f}_X(1) \gg 0 \quad (34)$$

(positive edge) or

$$0 \gg \bar{f}_X(-1) \gg \bar{f}_X(0), \quad \bar{f}_X(0) \ll \bar{f}_X(1) \ll 0 \quad (35)$$

(negative edge) are satisfied. The satisfaction of " \ll " and " \gg " are ascertained by a threshold on the difference between the two sides. The subpixel resolution is obtained by the quadratic fitting

$$X = \frac{1}{2} \cdot \frac{\bar{f}_X(1) - \bar{f}_X(-1)}{2\bar{f}_X(0) - \bar{f}_X(-1) - \bar{f}_X(1)}. \quad (36)$$

The edge position with respect to the center of Γ is $(X \cos \theta_{EG}, X \sin \theta_{EG})$.

3.1.3 Localization of Ridges from Zero-Crossing

Similarly, the zero-crossing is detected near the adjacent triple points which satisfy

$$\bar{f}_X(-1) \ll \bar{f}_X(0) \ll \bar{f}_X(1), \quad \bar{f}_X(-1)\bar{f}_X(1) < 0 \quad (37)$$

(negative ridge) or

$$\bar{f}_X(-1) \gg \bar{f}_X(0) \gg \bar{f}_X(1), \quad \bar{f}_X(-1)\bar{f}_X(1) < 0 \quad (38)$$

(positive ridge) by the quadratic fitting

$$X \simeq \frac{2\bar{f}_X(0)}{\bar{f}_X(-1) - \bar{f}_X(1)}. \quad (39)$$

The ridge position with respect to the center of Γ is also $(X \cos \theta_{EG}, X \sin \theta_{EG})$.

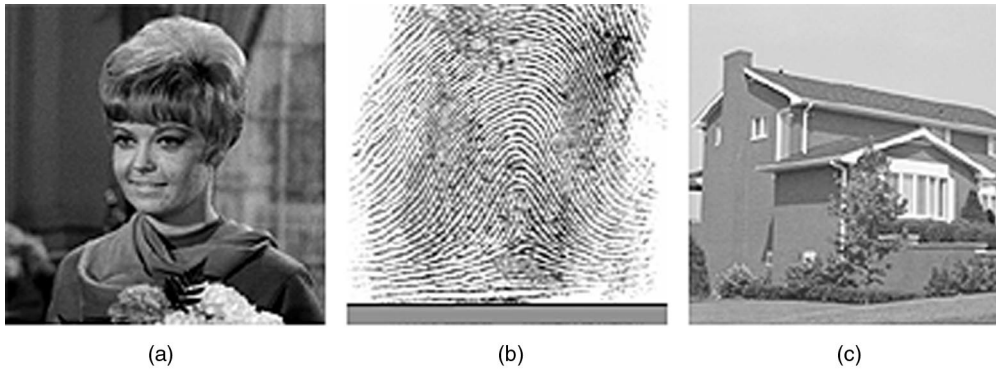


Fig. 6. Original images for the simulation of edge/corner localization. (a) "Girl" image. (b) "Fingerprint" image. (c) "Home" image. The size and the grayness of all images are 256×256 pixels and 8 bits, respectively.

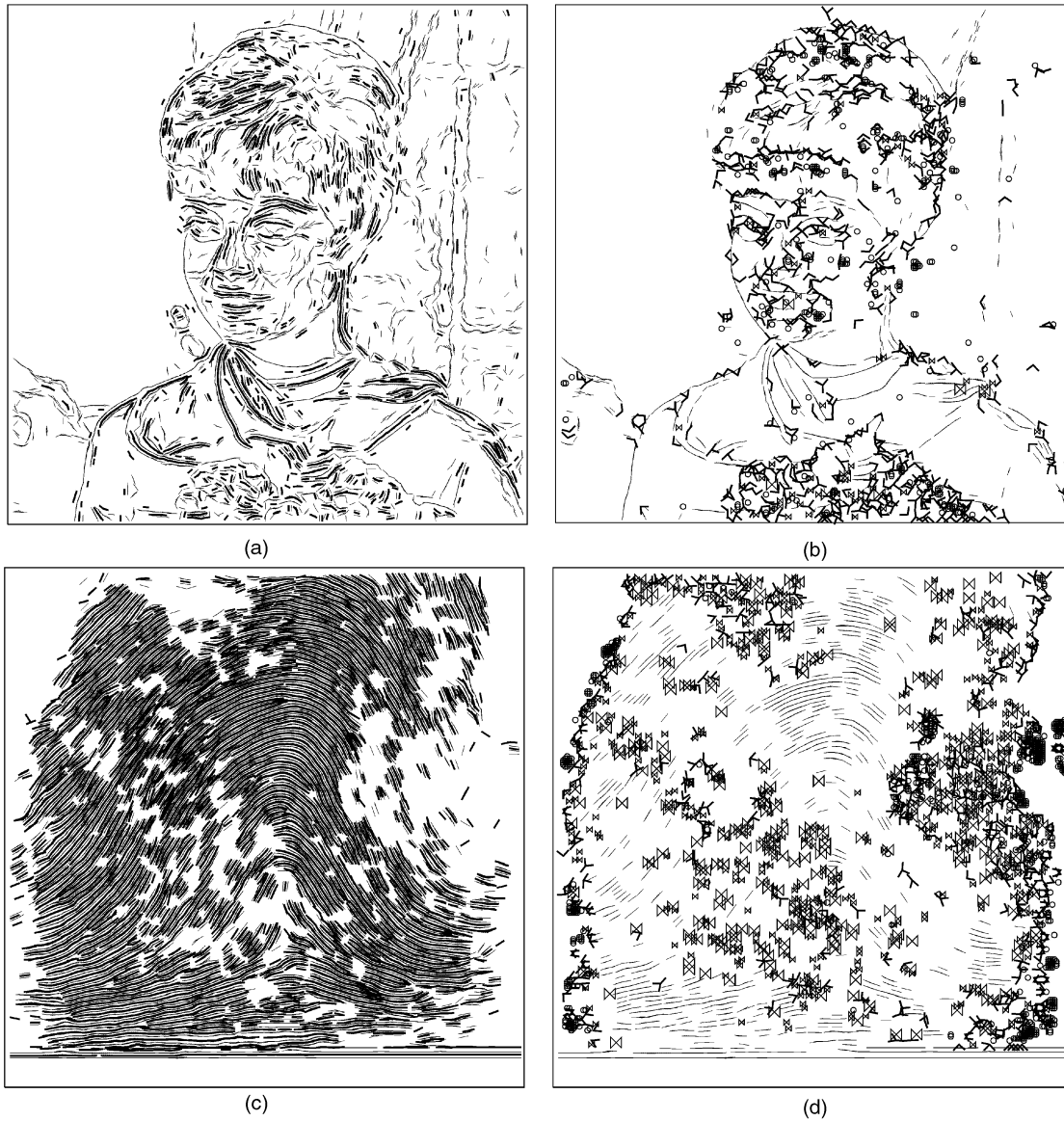


Fig. 7. An application of the edge/corner localization algorithm to various real images in Fig. 6a, Fig. 6b, Fig. 6c. The image size is 256×256 pixels and the grayness is 8 bits, Γ size is 3×3 , 5×5 , and 3×3 , and $\sigma_{EG}^2 = 3^2 \cdot 10.0, 5^2 \cdot 10.0$, and $3^2 \cdot 5.0$ for (a)-(b), (c)-(d), and (e)-(f), respectively. The extended Γ size is 7×7 , 9×9 , and 7×7 , respectively. (a), (c), and (e) Plots of detected edge segments (thin lines) and ridge segments (bold lines). (b), (d), and (f) Plots of detected corners (bold "L"s), vertices (bold "Y"s), X-junctions (small thin butterflies), and M-junctions (large thin butterflies). In (b), (d), and (f), edge segments which have P_{EG} larger than 0.9 are displayed for indicating the object shapes. For corners and vertices, the bold line segments indicate the directions of detected angular edges.

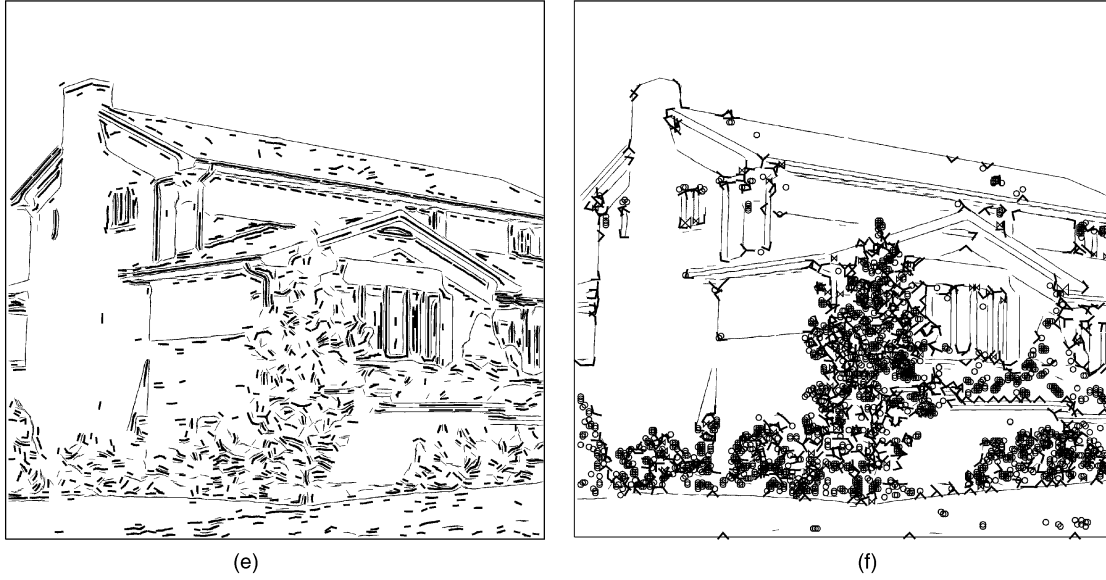


Fig. 7. Continued.

3.2 Corner/Vertex Localization by Angular Gradient Projection

The objectives of this procedure are 1) further classification of OMNIVAR into corners, vertices, and junctions, 2) their accurate localization, particularly of the corner where the maximum response of Q_{EG} has a significant offset, and 3) to give further attributes such as direction of edges around vertices. We propose a method based on radial projection of angular gradients on the polar coordinates because 1) it is the most informative axis of OMNIVAR, 2) the radial projection improves SNR of the informative axis without smearing, 3) projecting gradients simplifies the algorithm, i.e., cubic fitting to the grayness is performed by quadratic fitting to the gradient.

The actual implementation of the corner/vertex localization consists of the following steps.

3.2.1 Angular Gradient Projection

Let the polar coordinate be (ρ, θ) . Since the angular coordinate θ and the angular gradient f_θ are expressed as

$$\theta = \tan^{-1}\left(\frac{y}{x}\right), \quad f_\theta = \frac{yf_x - xf_y}{\sqrt{x^2 + y^2}}, \quad (40)$$

we can compute the gradient projection as

$$\bar{f}_\theta(\theta) = \frac{1}{L(\theta)} \int_{L(\theta)} \frac{yf_x - xf_y}{\sqrt{x^2 + y^2}} d\rho. \quad (41)$$

The definition of $L(\theta)$ is expressed in Fig. 5b. For small Γ , $L(\theta)$ is extended beyond Γ (e.g., two pixels in all sides for $3 \times 3 \Gamma$) so that a sufficient number of pixels lie under $L(x)$. Generally, obtaining $\bar{f}_\theta(\theta)$ discretely on $\theta = 2n\pi/N, n = 1, 2, \dots, N$ is sufficient (e.g., $N=16$). For simplicity, we express those values by $\bar{f}_\theta(n)$.

The above procedure is rather time-consuming, but the prior categorization by Q_{EG} greatly reduces the a number of locations on which to perform this procedure.

3.2.2 Detection of Edge Directions from Extrema

The gradient extrema are searched for $n = 1, 2, \dots, N$. At every point n , where

$$0 \ll \bar{f}_\theta(n-1) \ll \bar{f}_\theta(n), \quad \bar{f}_\theta(n) \gg \bar{f}_\theta(n+1) \gg 0 \quad (42)$$

(positive edge) or

$$0 \gg \bar{f}_\theta(n-1) \gg \bar{f}_\theta(n), \quad \bar{f}_\theta(n) \ll \bar{f}_\theta(n+1) \ll 0 \quad (43)$$

(negative edge) is satisfied, the quadratic fitting

$$\Delta = \frac{1}{2} \cdot \frac{\bar{f}_\theta(n+1) - \bar{f}_\theta(n-1)}{2\bar{f}_\theta(n) - \bar{f}_\theta(n-1) - \bar{f}_\theta(n+1)} \quad (44)$$

is used to obtain an interpolated result. The operations of $n-1$ and $n+1$ must be modulo N . The corresponding edge direction is $2\pi(n+\Delta)/N$. The number of detected edges is denoted by K .

3.2.3 Offset-Free Localization with Clarity Measure

The maxima of Q_{EG} have significant offset, particularly at the corners. To reduce the offset, we define a total energy measure of angular gradients as

$$V_\theta \equiv \int_0^{2\pi} \bar{f}_\theta(\theta)^2 d\theta, \quad (45)$$

where Q_{EG} has significant values, the maximum of V_θ is searched and interpolated to localize the corner and vertex with subpixel resolution.

3.2.4 Classification into Corner/Vertex/Junctions

The local maxima of V_θ are classified according to the number of edges K as follows:

$$\begin{cases} K \leq 1 & \text{peak or dip} \\ K = 2 & \text{corner} \\ K = 3 & \text{vertex} \\ K = 4 & \text{X-junction} \\ K \geq 5 & \text{M-junction} \end{cases} \quad (46)$$

Excepting peaks and dips, we can obtain the directions of all edges focusing to the point.

4 EXPERIMENTS

In the following experiments, smoothing and derivation in our approach is performed using Gaussian filtering with half a bandwidth of Nyquist frequency ($\sigma = \pi/2$) followed by Sobel gradient operators.

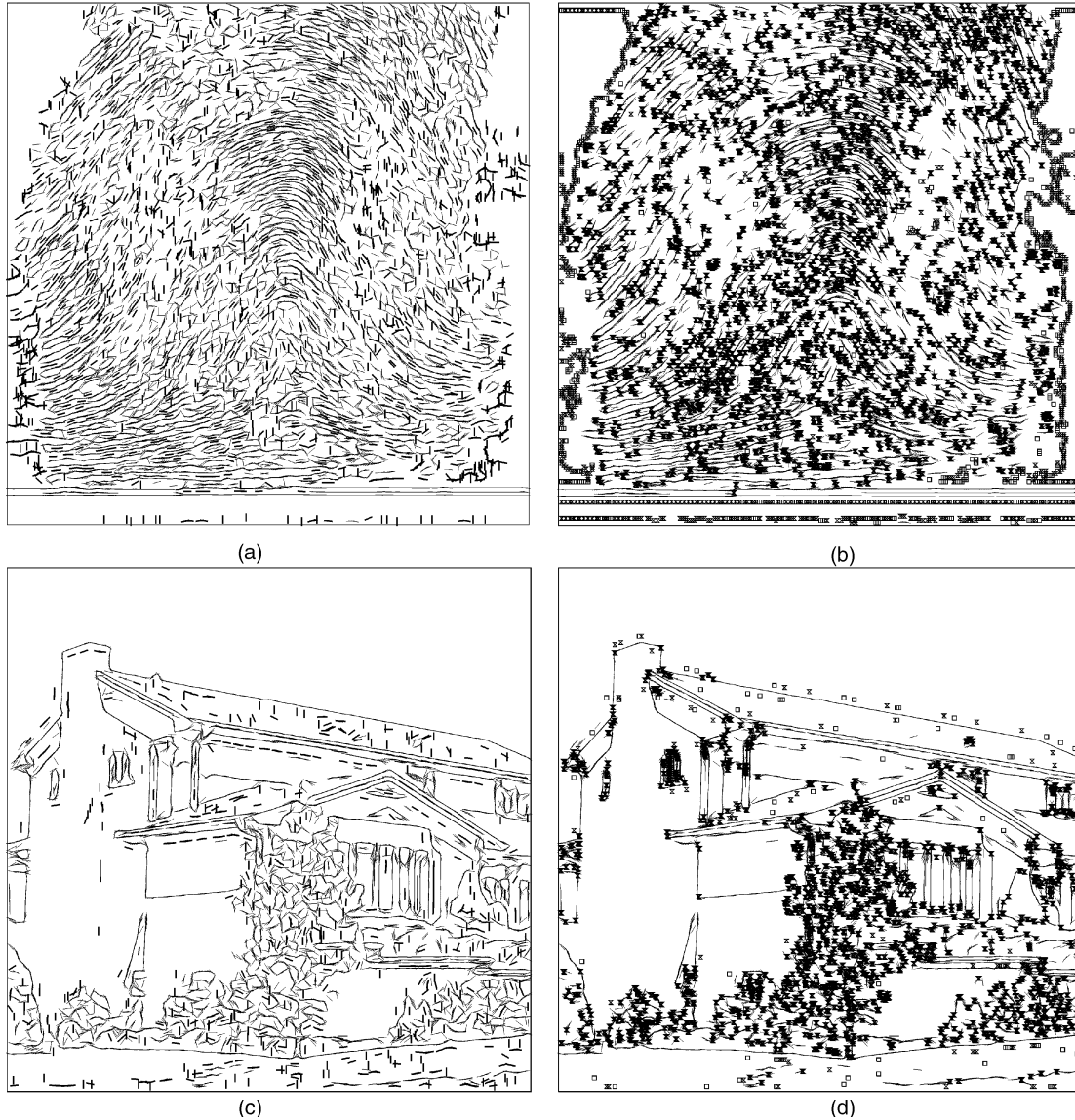


Fig. 8. An application of the differential operator method to images in Fig. 6b and Fig. 6c. The bandwidth of differential Gaussian filters is one-fourth of Nyquist frequency ($\sigma = \pi/4$). (a) and (c) Plots of detected edge segments (thin lines) and ridge segments (bold lines). (b) and (d) Plots of detected corners (bold large butterflies), peaks (thin rectangles), and saddles (small thin butterflies). In (b) and (d), edge segments are displayed for indicating the object shapes.

4.1 Performance of Overall Algorithms

Fig. 6a, Fig. 6b, and Fig. 6c represent various classes of real images, including the fingerprint pattern. Using our method with $\Gamma = 3 \times 3$, $\sigma_{EG}^2 = 3^2 \cdot 10.0$ for Fig. 6a, $\Gamma = 5 \times 5$, $\sigma_{EG}^2 = 5^2 \cdot 10.0$ for Fig. 6b, and $\Gamma = 3 \times 3$, $\sigma_{EG}^2 = 3^2 \cdot 5.0$ for Fig. 6c yields the results represented in Fig. 7a, Fig. 7b, Fig. 7c, Fig. 7d, Fig. 7e, and Fig. 7f. In (a) of each figure, detected edge segments and ridge segments are plotted as thin and bold lines, respectively. The length of one segment is equal to the Γ size. In (b) of each figure, detected corners, vertices, X-junctions, and M-junctions are plotted as bold "L"s, bold "Y"s, small thin butterflies, and large thin butterflies, respectively. In (b), edge segments which have P_{EG} larger than 0.9 are displayed for indicating the object shapes. For corners and vertices, the bold line segments of "L" and "Y" indicate the directions of detected angular edges.

Refer to Fig. 6a (standard "Girl" image) and Fig. 7a (edge/ridge map) and Fig. 7b (corner/vertex map). Almost all features have been well detected. Note that decreasing σ_{EG}^2 to less than $3^2 \cdot 10.0$ would have resulted in more feature points, although the number

of spurious ones increases due to image noise. From this result, we can contrast our method with other methods.

1. Resolution is good, because no prior smoothing is performed except for Gaussian filtering with $\sigma = \pi/4$ to reduce quantization noise.
2. Detected features are stable. This is, first, because the prior categorization by P_{EG} and Q_{EG} removes algorithmic ambiguities and, second, because averaging is performed along the least varying direction through projection. For the same reason,
3. spurious responses (false alarms) are few.
4. Curved edges of just a few pixels in diameter can be detected as a series of corners.

Next, refer to Fig. 6b ("Fingerprint" image) and Fig. 7c (edge/ridge map) and Fig. 7d (corner/vertex map). This image was chosen to demonstrate the resolution of the detector and the sensitivity to local defects involved in UNIVAR structure. In Fig. 7c, both edge detectors and ridge detectors successfully localize each line of the fingerprint although they are only three pixels wide.

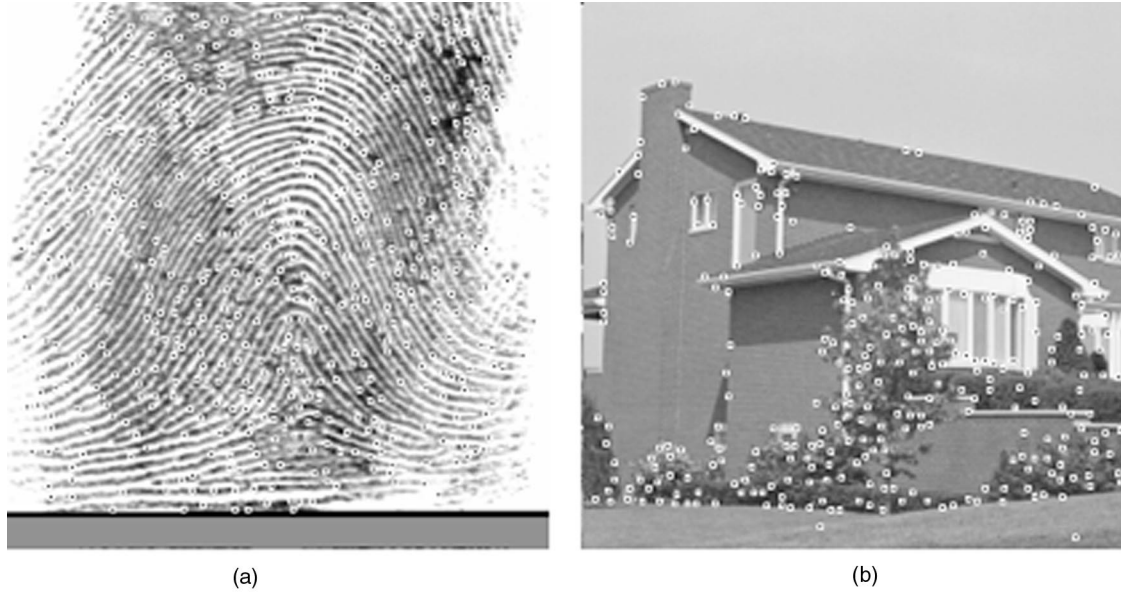


Fig. 9. The corner results of the SUSAN algorithm (<http://www.fmrib.ox.ac.uk/~steve/>). Corners of (a) "Fingerprint" image ($t = 20.0$) and (b) "Home" image ($t = 17.0$). See [31] or the above web site for the definition of grayness threshold t .

Note that negative ridges between stripes are also displayed. In Fig. 7d, the corner/vertex detector localizes junctions with large departure angle, terminals, and flaws along stripes. Although Q_{EG} often fails at smooth junctions at a small departure angle, they can be recognized in the edge/ridge map by P_{EG} .

Finally, refer to Fig. 6c ("Home" image) and Fig. 7e (edge/ridge map) and Fig. 7f (corner/vertex map). In Fig. 7e, the edge/ridge detectors extract well the frames of man-made structures continuously, and large textures of natural objects discontinuously. In Fig. 7f, the corner/vertex detectors localize the junctions of man-made structures and small textures of natural objects. For this image, we used $\sigma_{EG} = 3^2 \cdot 5.0$ because noise in this image was smaller than other two images. But, this caused some erroneous corners on the roof due to its texture. The choice of σ_{EG} should not only depend on noise levels, but also on the desired sensitivity of

how weak features must be detected.

4.2 Comparison with Other Methods

To compare our method with the differential operator method, first and second derivatives were computed by differential Gaussian filters. Then, 1) edges were detected through maximum search of gradient magnitude along the gradient direction, 2) corners were localized at the extrema of the isophotes curvature

$$C_{IP} = \frac{f_x^2 f_{xx} - 2 f_x f_y f_{xy} + f_y^2 f_{yy}}{(f_x^2 + f_y^2)^{3/2}} \quad (47)$$

along edges, 3) grayness extrema with sufficient squared average curvature were classified into ridges, peaks, and saddles according to the Gaussian curvature.

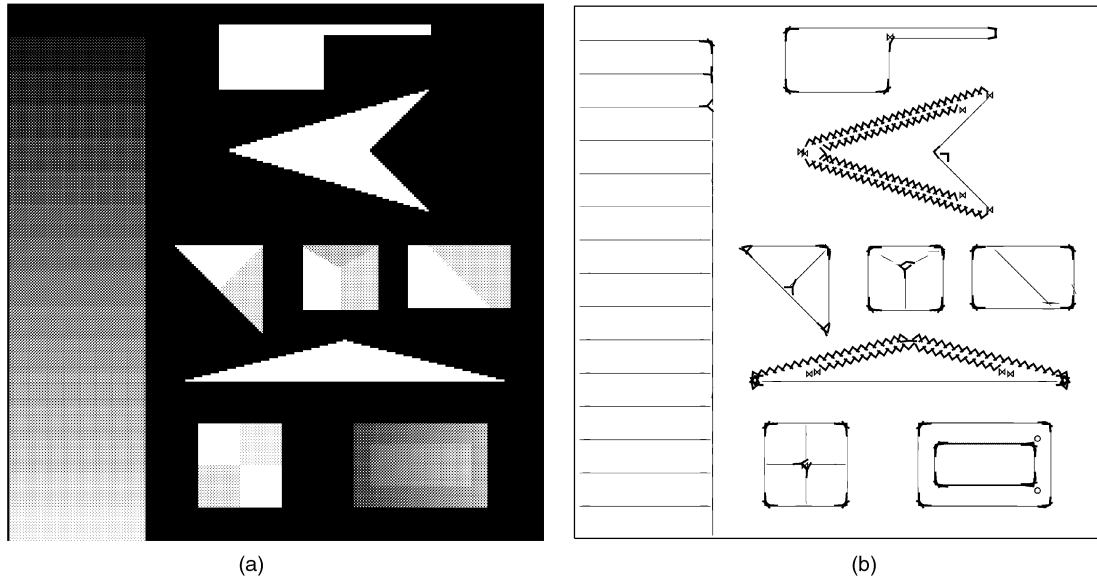


Fig. 10. An application of the edge/corner localization algorithm to a benchmark image (256×256 size, 8 bits grayness) of SUSAN method, by which all corners are perfectly detectable with a grayness threshold $t = 10.0$. In our method, we used 5×5 Γ size and $\sigma_{EG}^2 = 5^2 \cdot 2.0$. (a) A benchmark image. (b) Plots of detected edges (thin lines), corners (bold "L"s), vertices (bold "Y"s), X-junctions (small thin butterflies), and M-junctions (large thin butterflies).

TABLE 1
Comparison of Computation Time for 256×256 "Home" Image Using Sun Ultra 5 Workstation

method	differential filtering	feature extraction	neighborhood operation
proposed	0.85 s	0.20 s	0.86 s
differential	1.46 s	0.24 s	0.12 s
SUSAN[31]	5.52 s		1.70 s

Fig. 8 shows the results to the images shown in Fig. 6b and Fig. 6c. For both images, threshold selection on gradient and curvatures was a very critical job. In addition, excess sensitivity to local variation of gradients and curvatures were found. In Fig. 8a and Fig. 8b, the responses of edges and corners are strongly influenced by thickness fluctuation of fingerprints, whereas, in Fig. 7a and Fig. 7b, they are less influenced and the stripe shapes and their singularities are extracted more clearly. In Fig. 8c and Fig. 8d, spurious ridges, peaks, and saddles appear frequently at rising/falling edges of boundaries. Some spurious corners were detected on smeared edges caused by Gaussian smoothing. They show that differential operators alone are too local to provide sufficient information to identify them. Sophisticated neighborhood operations are always necessary. Contrarily, in our method, they are involved in the categorization and projection operations.

Fig. 9a and Fig. 9b show the results obtained by the SUSAN algorithm [31]. The results are very steady and moderate particularly in Fig. 9b. But, in Fig. 9a, the detected corners, for wide range of a parameter, do not always coincide with the singularities of stripe structures detected in Fig. 7d.

Fig. 10 shows an application of our algorithm to a SUSAN benchmark image [31]. Important differences are:

1. At some oblique sides of the triangles, edges are judged as series of corners.
2. At edges of steps of the gray scale, corners are not marked except for the darker area (upper side) although edges are fully detected.

The reason for 1 is the apparent zigzag pattern of the binarized shapes. The reason for 2 is in the prior classification of UNIVAR and OMNIVAR; junctions of a strong vertical edge and a weak horizontal edge are decidedly more likely to be UNIVAR (edges with some defects).

Table 1 shows a comparison of computation time. In the differential method, the time for higher order differentials is dominant. It is because the degree of smoothing ($\sigma = \pi/4$) is larger than the proposed method ($\sigma = \pi/2$) and additional calculations are required for the second order derivatives. In the proposed method, considerable time is spent for neighborhood operations, including projections, but the time for P_{EG} and Q_{EG} is not so large.

5 SUMMARY

We have proposed categorization operators of image field based on gradient covariance. The regions extracted by dimensionless thresholding of them were called UNIVAR and OMNIVAR, respectively. We showed that UNIVAR is a union of 1D patterns, like an edge and ridge, and OMNIVAR is frequently a union of 1D patterns in polar coordinates, like a peak, corner, and vertex. We then presented an algorithm to achieve further classification and localization of UNIVAR and OMNIVAR based on gradient projections along their less informative axis. The experimental results indicated the good performance of the proposed method in stability, localization, and resolution.

APPENDIX

Proof of Theorem 1.

1. Since $P_{EG} = 1 - Q_{EG}$, the absolute maximum of P_{EG} is achieved when $Q_{EG} = 0$. Using (6), this condition is expressed as

$$\begin{aligned} S_{xx}S_{yy} - S_{xy}^2 \\ = \iint_{\Gamma} f_x^2 dx dy \iint_{\Gamma} f_y^2 dx dy - \left(\iint_{\Gamma} f_x f_y dx dy \right)^2 \quad (48) \\ = 0. \end{aligned}$$

From Schwarz's inequality, the lefthand-side formula is nonnegative and the equality holds if and only if there exist constants a, b ($a^2 + b^2 \neq 0$) such that³

$$af_x + bf_y = 0 \quad \text{in } \Gamma. \quad (49)$$

Transforming the variables x, y into

$$X = -bx + ay, \quad Y = ax + by, \quad (50)$$

gives

$$\begin{aligned} f_x &= \frac{\partial X}{\partial x} f_X + \frac{\partial Y}{\partial x} f_Y = -bf_X + af_Y \\ f_y &= \frac{\partial X}{\partial y} f_X + \frac{\partial Y}{\partial y} f_Y = af_X + bf_Y, \end{aligned}$$

and we can rewrite (49) as

$$-abf_X + a^2f_Y + abf_X + b^2f_Y = (a^2 + b^2)f_Y = 0.$$

Hence, the condition in (X, Y) coordinates is expressed as

$$f_Y = 0 \quad \text{in } \Gamma. \quad (51)$$

Since f is continuously differentiable everywhere, this equation is solved as

$$f(X, Y) = g(X) \quad \text{in } \Gamma, \quad (52)$$

where $g(X)$ is an arbitrary differentiable function of X . Changing again the variables into x, y , we obtain

$$f(x, y) = g(-bx + ay) \quad \text{in } \Gamma, \quad (53)$$

which means that the grayness varies one-dimensionally in Γ .

2. Since $Q_{EG} = 1 - P_{EG}$, it is satisfied when $P_{EG} = 0$. Using (9), this condition is expressed as

$$S_{xx} = S_{yy}, \quad S_{xy} = 0, \quad (54)$$

or, equivalently, as

$$\iint_{\Gamma} f_x^2 dx dy = \iint_{\Gamma} f_y^2 dx dy, \quad \iint_{\Gamma} f_x f_y dx dy = 0. \quad (55)$$

Therefore, in this sense, the grayness varies equally and independently along x and y axes. \square

3. Generally, (49) is also valid even if f_x and f_y have discontinuities in Γ . The following arguments will, therefore, be extendable to a class of images which involves gradient discontinuities where the brightness curvature becomes infinity.

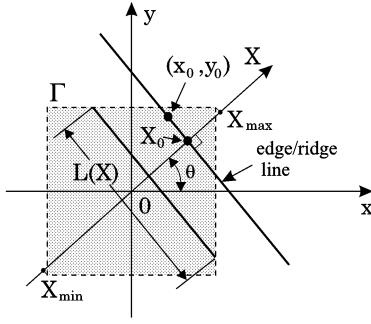


Fig. 11. Position and direction of an edge/ridge line with respect to those of the integration area Γ .

Proof of Observation 1.

1. From (14), it follows that $f_x = p$, $f_y = q$ everywhere in Γ . Thus, we obtain

$$S_{xx} + S_{yy} = \iint_{\Gamma} (p^2 + q^2) dx dy = L^2(p^2 + q^2) \quad (56)$$

and

$$S_{xx}S_{yy} - S_{xy}^2 = L^2p^2L^2q^2 - (L^2pq)^2 = 0, \quad (57)$$

where L^2 is an area of Γ . Therefore, the slant can be detected by P_{EG} when its gradient magnitude is

$$\sqrt{f_x^2 + f_y^2} = \sqrt{p^2 + q^2} \gg \sqrt{\frac{\sigma_{EG}^2}{L^2}}. \quad (58)$$

2. Let the edge/ridge line be

$$(x - x_0) \cos \theta + (y - y_0) \sin \theta = 0, \quad (59)$$

where θ is the normal direction of the line and (x_0, y_0) is a point on the line (see Fig. 11). Without loss of generality, we assume that the origin of the (x, y) coordinate is on a center of Γ . Let (X, Y) be a coordinate which is spanned by the normal of the line and the line itself and which has its origin at the center of Γ . Let the cross section of the edge/ridge be $g(\cdot)$. Then, from assumption 2, the grayness pattern is expressed as

$$\begin{aligned} f(x, y) &= g(x \cos \theta + y \sin \theta - x_0 \cos \theta + y_0 \sin \theta) \\ &= g(X - X_0), \end{aligned} \quad (60)$$

where

$$X_0 = x_0 \cos \theta + y_0 \sin \theta \quad (61)$$

is the displacement of the line with respect to the center of Γ . Clearly, this is the form of (53).

Using (60), we obtain

$$\begin{aligned} S_{xx} + S_{yy} &= \iint_{\Gamma} g_X((x - x_0) \cos \theta + (y - y_0) \sin \theta)^2 dx dy \\ &= \int_{X_{\min}}^{X_{\max}} L(X) g_X(X - X_0)^2 dX, \end{aligned}$$

where $[X_{\max}, X_{\min}]$ is an extent of Γ along the X coordinate and $L(X)$ is the length of the intersection of

the line $X = X_0$ with Γ . This shows that $S_{xx} + S_{yy}$, as a function of the displacement X_0 , gives a correlation of $g_X(X)^2$ with $L(X)$, whereas, from assumption 1, $g_X(X)^2$ is localized near the origin. Therefore, by assuming

$$g_X^2(X) \sim 0 \quad |X| > \epsilon, \quad (62)$$

where ϵ is a length which is sufficiently smaller than the size of Γ , we find

$$\begin{aligned} S_{xx} + S_{yy} &\sim \begin{cases} L(X_0) \int_{-\epsilon}^{\epsilon} g_X(X)^2 dX & (X_{\min} < X_0 < X_{\max}) \\ 0 & (\text{otherwise}). \end{cases} \end{aligned}$$

Therefore, if the magnitude of an edge or ridge is such that

$$\int_{-\epsilon}^{\epsilon} g_X(X)^2 dX \gg \frac{\sigma_{EG}^2}{L_{\max}}, \quad (63)$$

where L_{\max} is the maximum length of the intersection, P_{EG} reaches 1 near edges or ridges where

$$X_{\min} < X_0 < X_{\max}. \quad (64)$$

This means that it is a region where $P_{EG} \sim 1$ becomes a band along an edge or a ridge. The width of the band is about $X_{\max} - X_{\min}$ plus an actual width of the edge/ridge.

3. For simplicity, we assume here that Γ is a circle of radius R . Since

$$f_x = f_r \cos \theta - f_{\theta} \frac{\sin \theta}{r}, \quad f_y = f_r \sin \theta + f_{\theta} \frac{\cos \theta}{r} \quad (65)$$

in polar coordinates (r, θ) with an origin at the center of Γ , it follows, for circularly symmetric grayness with respect to a center of Γ , that

$$\begin{aligned} S_{xx} &= \int_0^R \int_0^{2\pi} f_r^2 \cos^2 \theta r dr d\theta = \pi \int_0^R r f_r^2 dr \\ S_{xy} &= \int_0^R \int_0^{2\pi} f_r^2 \frac{\sin 2\theta}{2} r dr d\theta = 0 \\ S_{yy} &= \int_0^R \int_0^{2\pi} f_r^2 \sin^2 \theta r dr d\theta = \pi \int_0^R r f_r^2 dr, \end{aligned}$$

by which (55) is satisfied. This shows that Q_{EG} reaches 1 at the center of a circularly symmetric pattern with a magnitude of variation of

$$S_{xx} + S_{yy} = 2\pi \int_0^R r f_r^2 dr \gg \sigma_{EG}^2. \quad (66)$$

The condition of circular Γ can be removed if most of the magnitude of variation is concentrated in a circle which is smaller than Γ .

4. Using (15), (16), and (17) ((18), (19), and (20) for 5)), we obtain

$$\begin{aligned} S_{xx} &= 2 \int_0^R \int_0^{\frac{\pi}{2}} \left(f_r^2 + \frac{f_{\theta}^2}{r^2} \right) r dr d\theta \\ S_{xy} &= 0 \\ S_{yy} &= 2 \int_0^R \int_0^{\frac{\pi}{2}} \left(f_r^2 + \frac{f_{\theta}^2}{r^2} \right) r dr d\theta, \end{aligned}$$

by which (55) is satisfied. This shows that Q_{EG} reaches 1 at a center of rotational periodicity with a period $\pi/2$, the magnitude of variation of which is

$$S_{xx} + S_{yy} = 4 \int_0^R \int_0^{\frac{\pi}{2}} \left(f_r^2 + \frac{f_\theta^2}{r^2} \right) r dr d\theta \gg \sigma_{EG}^2. \quad (67)$$

This observation shows that the condition of circular Γ can be released to a square Γ because it has a rotational symmetry with a period $\pi/2$. \square

REFERENCES

- [1] A. Rosenfeld and M. Thurston, "Edge and Curve Detection for Visual Scene Analysis," *IEEE Trans. Computers*, vol. 20, no. 5, pp. 562-569, 1971.
- [2] G. Robinson, "Edge Detection by Compass Gradient Masks," *Computer Graphics Image Processing*, vol. 6, pp. 492-501, 1977.
- [3] W. Frei and C.-C. Chen, "Fast Boundary Detection: A Generalized and a New Algorithm," *IEEE Trans. Computers*, vol. 26, no. 10, pp. 988-998, Oct. 1977.
- [4] K.S. Shanmugam, F.M. Dickey, and J.A. Green, "An Optimal Frequency Domain Filter for Edge Detection in Digital Pictures," *IEEE Trans. Pattern Analysis and Machine Intelligence*, vol. 1, no. 1, pp. 37-49, 1979.
- [5] R. Nevatia and K.R. Babu, "Linear Feature Extraction and Description," *Computer Vision Graphics Image Processing*, vol. 13, pp. 257-269, 1980.
- [6] D. Marr and E.C. Hildreth, "Theory of Edge Detection," *Proc. Royal Soc. London, B*, vol. 207, pp. 187-217, 1980.
- [7] J.F. Canny, "A Computational Approach to Edge Detection," *IEEE Trans. Pattern Analysis and Machine Intelligence*, vol. 8, no. 6, pp. 679-698, 1986.
- [8] G. Ramponi, "Edge Extraction by a Class of Second-Order Nonlinear Filters," *Electronics Letters*, vol. 22, no. 9, pp. 482-484, 1986.
- [9] M. Kisworo, S. Venkatesh, and G. West, "Modeling Edges at Subpixel Accuracy Using the Local Energy Approach," *IEEE Trans. Pattern Analysis and Machine Intelligence*, vol. 16, no. 4, pp. 405-410, Apr. 1994.
- [10] R. Machuca and A.L. Gilbert, "Finding Edges in Noisy Scenes," *IEEE Trans. Pattern Analysis and Machine Intelligence*, vol. 3, no. 1, pp. 103-111, 1981.
- [11] O.A. Zuniga and R.M. Haralick, "Integrated Directional Derivative Gradient Operator," *IEEE Trans. Systems, Man, and Cybernetics*, vol. 17, no. 3, pp. 508-517, 1987.
- [12] P.H. Gregson, "Using Angular Dispersion of Gradient Direction for Detecting Edge Ribbons," *IEEE Trans. Pattern Analysis and Machine Intelligence*, vol. 15, no. 7, pp. 682-696, 1993.
- [13] J.-B. Martens, "Local Orientation Analysis in Images by Means of the Hermite Transform," *IEEE Trans. Image Processing*, vol. 6, no. 8, pp. 1,103-1,116, 1997.
- [14] M. Brooks, "Rationalizing Edge Detector," *Computer Vision Graphics Image Processing*, vol. 8, pp. 277-285, 1978.
- [15] R.M. Haralick, "Digital Step Edges from Zero-Crossings of Second Directional Derivatives," *IEEE Trans. Pattern Analysis and Machine Intelligence*, vol. 6, no. 1, pp. 58-68, 1984.
- [16] A.J. Tabatabai and O.R. Mitchell, "Edge Location to Subpixel Values in Digital Imagery," *IEEE Trans. Pattern Analysis and Machine Intelligence*, vol. 6, no. 2, pp. 188-201, 1984.
- [17] V.S. Nalwa and T.O. Binford, "On Detecting Edges," *IEEE Trans. Pattern Analysis and Machine Intelligence*, vol. 8, no. 6, pp. 699-714, 1986.
- [18] S. Ghosal and R. Mehrotra, "Detection of Composite Edges," *IEEE Trans. Image Processing*, vol. 3, no. 1, pp. 14-25, 1994.
- [19] G. Chen and Y.H.H. Yang, "Edge Detection by Regularized Cubic B Spline Fitting," *IEEE Trans. Systems, Man, and Cybernetics*, vol. 25, no. 4, pp. 635-642, 1995.
- [20] L. Kitchen and A. Rosenfeld, "Gray-Level Corner Detection," *Pattern Recognition Letters*, vol. 1, pp. 95-102, 1982.
- [21] J.A. Noble, "Finding Corners," *Image and Vision Computing*, vol. 6, pp. 121-128, 1988.
- [22] K. Rangarajan, M. Shah, and D.V. Brackley, "Optimal Corner Detector," *Computer Vision, Graphics, and Image Processing*, vol. 48, pp. 230-245, 1989.
- [23] A. Singh and M. Shneier, "Gray Level Corner Detection: A Generalized and Robust Real Time Implementation," *Computer Vision, Graphics, and Image Processing*, vol. 51, pp. 54-59, 1990.
- [24] R. Deriche and G. Giraudon, "A Computational Approach for Corner and Vertex Detection," *Int'l J. Computer Vision*, vol. 10, no. 2, pp. 101-124, 1993.
- [25] J. Cooper, S. Venkatesh, and L. Kitchen, "Early Jump-Out Corner Detectors," *IEEE Trans. Pattern Analysis and Machine Intelligence*, vol. 15, no. 8, pp. 823-828, 1993.
- [26] S. Ghosal and R. Mehrotra, "A Moment Based Unified Approach to Image Feature Detection," *IEEE Trans. Image Processing*, vol. 6, no. 6, pp. 781-793, 1997.
- [27] R. Machuca and K. Phillips, "Applications of Vector Fields to Image Processing," *IEEE Trans. Pattern Analysis and Machine Intelligence*, vol. 5, no. 3, pp. 316-329, 1983.
- [28] L.M.T. Florack, B.H. Romeny, J.J. Koenderink, and M.A. Viergever, "General Intensity Transformation and Differential Invariants," *J. Math. Imaging and Vision*, vol. 4, no. 2, pp. 171-187, 1994.
- [29] J.B.A. Maintz, P.A. van den Elsen, and M.A. Viergever, "Evaluation of Ridge Seeking Operators for Multimodality Medical Image Matching," *IEEE Trans. Pattern Analysis and Machine Intelligence*, vol. 18, no. 4, pp. 353-365, Apr. 1996.
- [30] C. Schmid and R. Mohr, "Local Grayvalue Invariants for Image Retrieval," *IEEE Trans. Pattern Analysis and Machine Intelligence*, vol. 19, no. 5, pp. 530-535, May 1997.
- [31] S.M. Smith and J.M. Brady, "SUSAN—A New Approach to Low Level Image Processing," *Int'l J. Computer Vision*, vol. 23, no. 1, pp. 45-78, 1997.
- [32] E. Deutsch and J. Fram, "A Quantitative Study of the Orientation Bias of Some Edge Detector Schemes," *IEEE Trans. Computers*, vol. 27, no. 3, pp. 205-213, Mar. 1978.
- [33] T. Peli and D. Malah, "A Study of Edge Detection Algorithm," *Computer Graphics and Image Processing*, vol. 20, pp. 1-21, 1982.
- [34] E.J. Delp and C.H. Chu, "Detecting Edge Segments," *IEEE Trans. Systems, Man, and Cybernetics*, vol. 15, no. 1, pp. 144-152, 1985.
- [35] E.P. Lyvers and O.R. Mitchell, "Precision Edge Contrast and Orientation Estimation," *IEEE Trans. Pattern Analysis and Machine Intelligence*, vol. 10, no. 6, pp. 927-937, 1988.
- [36] M.M. Fleck, "Some Defects in Finite-Difference Edge Finders," *IEEE Trans. Pattern Analysis and Machine Intelligence*, vol. 14, no. 3, pp. 337-345, Mar. 1992.
- [37] R. Kakarala and A.O. Hero, "On Achievable Accuracy in Edge Localization," *IEEE Trans. Pattern Analysis and Machine Intelligence*, vol. 14, no. 7, pp. 777-781, 1992.
- [38] J. Koplowitz and V. Greco, "On the Edge Location Error for Local Maximum and Zero-Crossing Edge Detectors," *IEEE Trans. Pattern Analysis and Machine Intelligence*, vol. 16, no. 12, pp. 1,207-1,212, Dec. 1994.
- [39] L. Ganesan and P. Bhattacharyya, "Edge Detection in Untextured and Textured Images—A Common Computational Framework," *IEEE Trans. Systems, Man, and Cybernetics*, vol. 27, no. 5, pp. 823-834, 1997.
- [40] F. Pedersini, A. Sarti, and S. Tubaro, "Estimation and Compensation of Subpixel Edge Localization Error," *IEEE Trans. Pattern Analysis and Machine Intelligence*, vol. 19, no. 11, pp. 1,278-1,284, Nov. 1997.
- [41] M. Heath, S. Sarkar, T. Sanocki, and K. Bowyer, "Comparison of Edge Detectors: A Methodology and Initial Study," *Computer Vision, Graphics, and Image Understanding*, vol. 69, no. 1, pp. 38-54, 1998.
- [42] S. Ando, "Texton Finders Based on Gaussian Curvatures of Correlation Functions," *IEEE Int'l Conf. Systems, Man, and Cybernetics*, pp. 25-28, Beijing/Shenyang, People's Republic of China, 1988.
- [43] S. Ando, "Image Feature Extraction Operators Based on Gaussian Curvature of Correlation Functions," *Trans. Soc. Instrumentation and Control Engineers*, vol. 24, no. 10, pp. 1,016-1,022, 1988 (in Japanese).
- [44] S. Ando, "An Intelligent Three-Dimensional Vision Sensor with Ears," *Sensors and Materials*, vol. 7, no. 3, pp. 213-231, 1995.
- [45] S. Ando, "An Autonomous Three-Dimensional Vision Sensor with Ears," *Trans. IEICE Information and Systems*, vol. E78-D, no. 12, pp. 1,621-1,629, 1995.